IOP Publishing | Institute of Physics and Engineering in Medicine Physics in Medicine & Biology

Phys. Med. Biol. **61** (2016) 3527–3539 doi:10.1088/0031-9155/61/9/3527

Minimal skin dose increase in longitudinal rotating biplanar linac-MR systems: examination of radiation energy and flattening filter design

A Keyvanloo[1], B Burke[1], J St. Aubin[1,2], D Baillie[1,2], K Wachowicz[1,2], B Warkentin[1,2], S Steciw[1,2] and B G Fallone[1,2]

[1] Department of Medical Physics, Cross Cancer Institute, 11560, University Avenue, Edmonton, Alberta, T6G 1Z2, Canada
[2] Department of Oncology, University of Alberta, 11560, University Avenue, Edmonton, Alberta, T6G 1Z2, Canada

E-mail: amir.keyvanloo@albertahealthservices.ca

Received 1 September 2015, revised 24 February 2016
Accepted for publication 4 March 2016
Published 6 April 2016

Abstract

The magnetic fields of linac-MR systems modify the path of contaminant electrons in photon beams, which alters patient entrance skin dose. Also, the increased SSD of linac-MR systems reduces the maximum achievable dose rate. To accurately quantify the changes in entrance skin dose, the authors use EGSnrc Monte Carlo calculations that incorporate 3D magnetic field of the Alberta 0.5 T longitudinal linac-MR system. The Varian 600C linac head geometry assembled on the MRI components is used in the BEAMnrc simulations for 6 MV and 10 MV beam models and skin doses are calculated at an average depth of 70 μm using DOSXYZnrc. 3D modeling shows that magnetic fringe fields decay rapidly and are small at the linac head. SSDs between 100 and 120 cm result in skin-dose increases of between ~6%–19% and ~1%–9% for the 6 and 10 MV beams, respectively. For 6 MV, skin dose increases from ~10.5% to ~1.5% for field-size increases of $5 \times 5\,\text{cm}^2$ to $20 \times 20\,\text{cm}^2$. For 10 MV, skin dose increases by ~6% for a $5 \times 5\,\text{cm}^2$ field, and decreases by ~1.5% for a $20 \times 20\,\text{cm}^2$ field. Furthermore, the proposed reshaped flattening filter increases the dose rate from the current 355 MU min^{-1} to 529 MU min^{-1} (6 MV) or 604 MU min^{-1} (10 MV), while the skin-dose increases by only an additional ~2.6% (all percent increases in skin dose are relative to D_{max}). This study suggests that there is minimal increase in the entrance skin dose and minimal/no decrease in the dose rate of the Alberta

longitudinal linac-MR system. The even lower skin dose increase at 10 MV offers further advantages in future designs of linac-MR prototypes.

Keywords: Monte Carlo, skin dose, electron contamination, longitudinal linac-MR, 3D MRI field

(Some figures may appear in colour only in the online journal)

1. Introduction

Currently, there are two integrated linear accelerator/magnetic resonance imager (linac-MRI) prototypes that allow real-time imaging during linac radiation (Fallone *et al* 2009, Raaymakers *et al* 2009), with two more under construction (Keall *et al* 2014, Heid *et al* 2015).These systems aim to provide the accurate soft tissue contrast required for real-time tumour tracking, leading to the potential reduction in treatment margins.

The linac-MR prototype in Raaymakers *et al* (2009) consists of a modified 1.5 T Achieva Phillips (Best, The Netherlands) MRI integrated with an Elekta (Stockholm, Sweden) 8 MV accelerator. In this configuration the MRI is a typical cylindrical bore magnet where the main magnetic field lies parallel to the patient superior–inferior (sup–inf) axis. The linear accelerator is mounted outside the cylinder and rotates around it, thus the radiation beam is perpendicular to the main magnetic field direction.

Our research group's system incorporates a rotating biplanar (RBP) magnet with field strengths, originally of 0.2 T (Fallone *et al* 2009) and currently 0.5 T (St. Aubin *et al* 2010a, Santos *et al* 2012, Fallone 2014). This allows two configurations for the direction of the radiation beam with respect to the magnetic field; perpendicular for the transverse case (Kirkby *et al* 2008, Fallone *et al* 2009, Fallone 2014), and parallel for the longitudinal case (Kirkby *et al* 2010, Fallone 2014).

The magnetic field of linac-MR systems causes dose distribution perturbations as a result of the action of the Lorentz force on electrons. The different effects have been explained and evaluated in several publications (Raaymakers *et al* 2004, 2005, 2008, Kirkby *et al* 2008, 2010). One of these effects is on patient skin dose, which is the focus of this work.

Skin dose has been shown to be significantly altered by the presence of the MRI magnetic field (Raaijmakers *et al* 2007, Oborn *et al* 2009, 2010, 2012, 2014, Keyvanloo *et al* 2012, Van Heijst *et al* 2013). This is as a result of changes in the path of contaminant electrons, which are the major contributor to skin dose. There is no increase in skin dose for transverse systems at direct incidence as the contaminant electrons are swept from the beam path (Keyvanloo *et al* 2012). However, these systems can suffer higher exit doses because the electrons ejected from the exit surface are forced back to the exit surface due to the Lorentz force in a condition known as the electron return effect (ERE) (Raaijmakers *et al* 2007, Oborn *et al* 2009, 2010, Keyvanloo *et al* 2012). The increased exit dose can manifest as a higher dose to the patient skin in cases such as whole breast irradiation (Van Heijst *et al* 2013).

In the longitudinal configuration some of the contaminant electrons, which would normally scatter outside the beam path, are instead confined within the beam and contribute to higher entrance skin dose (Keyvanloo *et al* 2012, Oborn *et al* 2012, 2014). Our previous work showed that for our previous system (v1: Alberta rotating whole-body linac-MR, 0.5 T, 6 MV-figures available on linacMR.ca), the increase in skin dose in all simulated field sizes and source to surface distances (SSDs) was no greater than 15%, relative to the dose at d_{max} (Keyvanloo *et al* 2012). Other authors have shown that proposed systems may have a severely increased skin dose, up to 1400% of d_{max} dose for a $20 \times 20\,cm^2$ field size and have suggested methods

to mitigate this (Oborn *et al* 2014). The major reason for this extremely large difference in the reported skin dose of these systems is the magnitude of the MRI fringe field components at the linac head. The large fringe field of the magnet reported by Oborn *et al* (2014) is shown to capture contaminant electrons and direct them towards the phantom surface. For the 160 cm source to axis distance (SAD) geometry they described, a fringe field of up to ~0.1 T is seen at the position of the multileaf collimator (MLC) at 45 cm below the target (figure 3 in Oborn *et al* 2014). However, our previous system (Keyvanloo *et al* 2012) has a fringe field of ~0.0025 T at the position of the MLC which is also at 45 cm below the target.

Since all proposed linac-MR systems have an increased SAD, an important consideration for these systems is the reduction in dose rate at isocenter. The increased SAD of linac-MR systems, from the standard 100 cm to 126 cm (Keyvanloo *et al* 2012), 147 cm (Crijns *et al* 2012), and 160 cm (Oborn *et al* 2014), will lead to reductions of 37%, 54%, and 61%, respectively, due to the inverse square effect. As a consequence, increased patient treatment times would be required. By operating without a flattening filter the dose rate can be increased; however, as will be shown, this exacerbates increases in the skin dose resulting from the presence of a longitudinal magnetic field. This suggests that a redesigned flattening filter may provide the best compromise between maximizing dose rate and minimizing increases in skin dose.

This work investigates important design considerations with respect to skin dose and dose rate for our current linac-MR system (v2), which is described for the first time in this paper (section 2.1). Skin dose of the v2 system will be quantified for both a standard 6 MV accelerator (St. Aubin *et al* 2010b), and for a novel short 10 MV accelerator designed by our group (Baillie *et al* 2015). Skin dose and dose rate for both energies are compared to those on a standard linac (where the magnetic field is absent) for three flattening filter configurations: original, redesigned, and removed. In this way, the significance of beam energy and flattening filter design are quantified.

2. Materials and methods

2.1. V2 design advantages

A schematic of the v2 linac-MR is shown in figure 1. Our v2 design is a 0.5 T longitudinal system with an SAD of 130 cm and a standard, unmodified Varian 600C linac head. Although similar, the v2 design differs from our previous system (v1) (Keyvanloo *et al* 2012) in both the geometry of the linac head and its magnet design The v1 had a slightly shorter SAD of 126 cm and used a modified 600C linac head, where the light mirror was removed and the jaws moved closer to the target. As seen in figure 2, the magnet yoke structure in the v2 design is now shaped to allow the linac to be as close to isocenter as possible. This is achieved by hollowing out the section of the yoke beneath the linac and making the edges of the yoke structure thicker. Both of these differences provide a potential advantage of decreasing the geometric penumbra for v2 compared to v1 through reduction in source magnification as the multileaf collimators are moved into the hollow space in the yoke structure of v2, thus moving them further away from the target.

Differences in the magnet and yoke design between the two prototypes will also change the MRI fringe field experienced by the linac head, potentially altering the skin dose. The increase in the skin dose due to the magnetic field of v2 is investigated in this work to determine if it remains clinically acceptable.

The increased SAD (130 cm) of our system will reduce the dose rate at isocenter. As a potential solution to this reduction, we first investigated removing the flattening filter. However, as shown in section 3, this resulted in a significant increase in the skin dose. Thus, in order

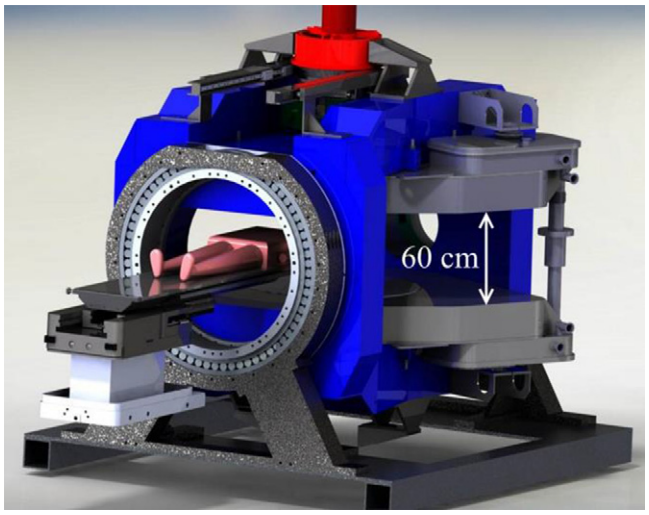

Figure 1. A schematic of the v2 linac-MR system with patient opening of 110 cm in diameter and pole to pole separation of 60 cm, as highlighted.

to maximize the achievable dose rate while minimizing the skin dose, we endeavoured to reshape the flattening filter. In our v2 system, the field size is limited by the hole size (25 cm) in the magnet and yoke structure. This means that the standard flattening filter is wider and thicker than necessary. The flattening filter was reshaped by truncating the edges to match the maximum required field size. This allowed the thickness of the flattening filter to be reduced by removing a uniform layer at the bottom, such that the thickness of the new filter decreased to zero at its new edges. This was done for the 6 MV and for the 10 MV systems.

2.2. Magnetic field simulation

A magnet yoke was designed to accommodate a 0.5 T bi-planar MRI magnet, with an intended pole to pole separation of 60 cm (figure 2). The yoke was designed with 1020 steel, with the exception of the pole plates which were designed with grain-oriented silicon steel. The assumed B-H relationships are given in figure 3. Data for the 1020 steel were compiled based on two published sources (Gloria *et al* 2009, Brauer 2013), and the data for the silicon steel were taken from product documentation from AK steel (M-2 MILL-ANNEAL grain-oriented electrical steel). The magnetic field was generated with two 179 kA current loops having a mean radius of 78.6 cm, and a vertical displacement of $\pm$42.5 cm from isocenter. This design allows the linac radiation to be along the direction of the magnetic field. To this end, a 24 cm diameter portal was integrated into the pole plate to allow the radiation to pass unobstructed. Above one of the magnet poles there are steel pieces designed to reduce stray magnetic fields at the site of the linac target, as well as the accelerating waveguide. In this design, the top of the yoke structure (above the pole) was 70 cm from isocentre, allowing the linac target to be positioned 130 cm from isocentre. In order to generate the resulting magnetic-field distribution, a finite element method (FEM) analysis of the yoke was conducted using Opera 3D commercial software (Cobham, Kidlington, UK). An outer cubic boundary with a dimension of 30 m, being large enough to contain the vast majority of magnetic field fluctuations was assigned the boundary condition $\overline{B} \cdot \hat{n} = 0$ A symmetric model was then assumed in the z direction to reduce the number of mesh points by only considering the model in the $z > 0$

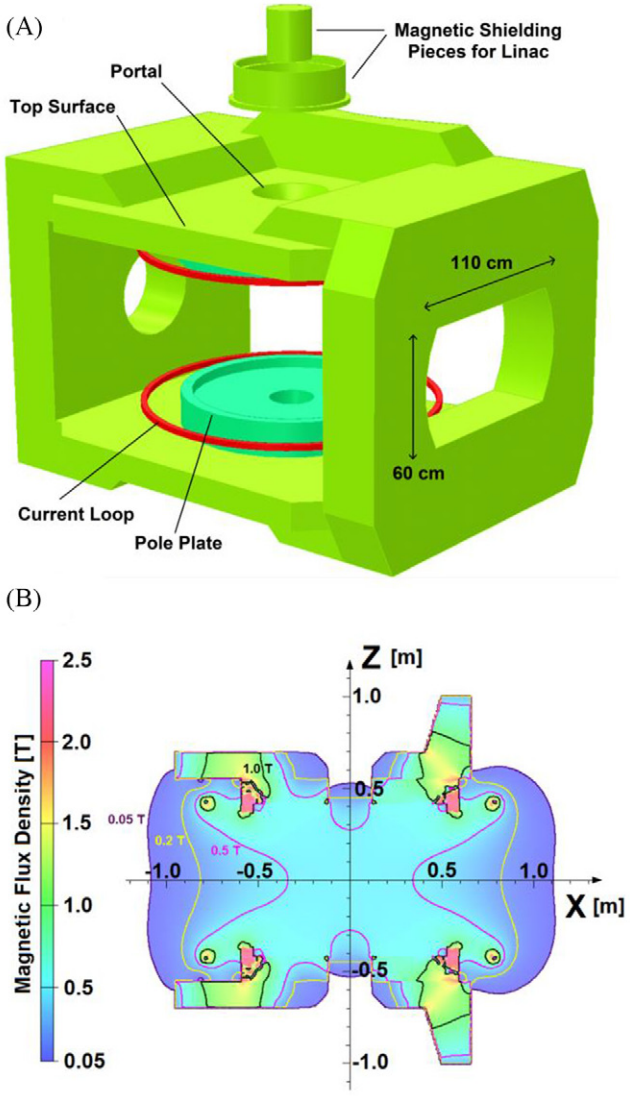

Figure 2. (A) Structural layout of the magnet yoke, composed of 1020 stainless steel. Stainless steel pieces were also included to attenuate the magnetic field in the linac region. The pole plates, modelled with grain-oriented Si Steel, are represented with a darker colour. The location and size of the superconducting current loops are also illustrated. (B) A contour plot of the magnetic field distribution within the MR unit, ranging between 0.05 and 2.5 T. All axis labels are in units of meters.

domain. The boundary condition over the $z = 0$ plane was then $B_{\text{Tangential}} = 0$. The total model mesh consisted of roughly 1.1 million nodes. A Newton–Raphson method was applied to converge to a solution, which met our stopping criteria within 17 iterations and over a duration of 83 min. The resulting magnetic vector field solution was regridded with 1 cm resolution over a 3D rectangular volume and exported for analysis. This volume spanned 130 cm from the target to isocentre, and 60 cm in both lateral Cartesian dimensions. The 3D directionality

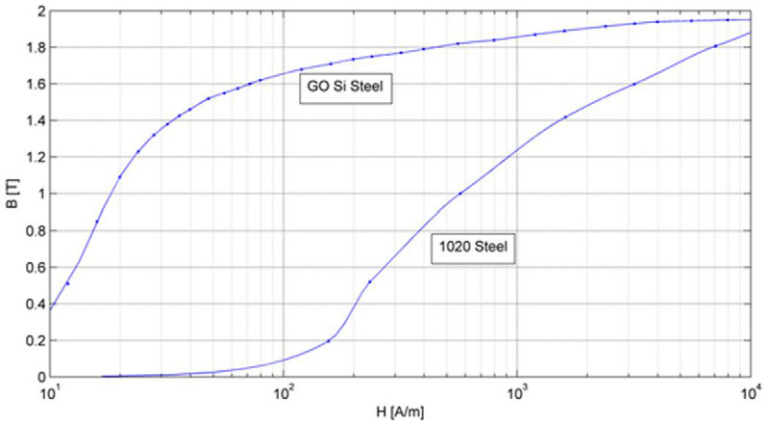

Figure 3. B-H relationships for the two materials used in the FEM magnetic field simulation.

of the field was preserved throughout the analysis process as this information is critical to ensuring accurate electron trajectories, particularly in the fringe field region (figure 3).

2.3. 10 MV linac design

Our group previously designed a short klystron-powered 10 MV S-band linac for use with our linac-MR system (Baillie *et al* 2015). Despite using higher electric fields than conventional 6 MV linacs of this size, our 10 MV linac is designed to avoid electric breakdown within the waveguide accelerator, which would reduce the output and ultimately damage the accelerator. Using an energy of 10 MV could provide dosimetric benefits for treatment sites with deep seated tumours or for anatomy with large separations due to its decreased surface doses and greater penetration. Tumour sites that may benefit from the higher energy include prostate, cervix, and breast.

2.4. Monte Carlo simulations

All Monte Carlo simulations were performed using BEAMnrc and DOSXYZnrc radiation transport codes together with an in-house modified version of emf_macros to account for the change in charged particle transport by magnetic fields (Bielajew 1989, 1993, Kawrakow and Rogers 2003, Rogers *et al* 2005, Walters *et al* 2005, Kirkby *et al* 2008, 2010, Keyvanloo *et al* 2012). The Monte Carlo calculations were run on either the western Canada research grid (WestGrid) computing clusters, employing hundreds of processors, or using an in-house cluster comprised of 192 processors. For the generation of the phase space files used in the DOSXYZnrc simulations, the BEAMnrc simulations included the linac head geometries, all magnet-related structures, and the 3D magnetic field. Inputs into the BEAMnrc transport code were derived from a six dimensional (6D) electron phase space calculated at the target from our 6 MV and 10 MV linac simulations (St. Aubin *et al* 2010b, Baillie *et al* 2015). In order to determine the increase in skin dose at both 6 MV and 10 MV, the 6D phase space from our linac simulations were used with our v2 linac-MR system with an SAD of 130 cm, as well as for conventional linac head models with a 100 cm SAD. The electrons contamination paths were tracked and saved into an 'egsgph' file through the use of a parameter IWATCH = 4 in

the BEAMnrc simulations. The EGS_Windows package (Treurniet *et al* 1999) was then used to visualize the trajectories of these electrons both in the absence and the presence of the 3D magnetic field of the v2 linac-MR system.

The first parameter investigated in the analysis was the air gap, which is defined as the distance between the phantom surface and the bottom of the magnet pole (see figure 3(a) in Keyvanloo *et al* (2012)). The BEAMnrc phase space files were scored at 95 cm from the target for a field size of $10 \times 10\,\text{cm}^2$ in the v2 model, using 3 billion particle histories. The effect of varying the air gap on skin dose was evaluated by running DOSXYZnrc and scoring dose distributions in a $30 \times 30 \times 30\,\text{cm}^2$ water phantom. Each simulation used 30 billion particle histories, resulting in statistical uncertainties of less than 1% for all voxels within the beam region and specifically less than 0.3% for the 70 μm voxels where skin doses are reported. Air gaps of 5, 10, 15, 20 and 25 cm were simulated, corresponding to SSDs of 100, 105, 110, 115 and 120 cm. The central axis (CAX) percent depth dose (PDD) was scored using a voxel size of $1 \times 1\,\text{cm}^2 \times 35$ μm in the first layer from the surface, followed by voxel sizes of $1 \times 1\,\text{cm}^2 \times 70$ μm to a depth of 2.8 cm and then $1 \times 1 \times 0.1\,\text{cm}^3$ at greater depths. The skin dose values were extracted at a depth of 70 μm (corresponding to the voxel encompassing depths between 35 μm and 105 μm), consistent with the recommendations of ICRP Publication 60 (ICRP 1991). Throughout this work the reported percent increases in skin dose are relative to $D_{\max}$.

To study the dependence of skin dose on field size, phase spaces were also generated for sizes of 5×5, 15×15 and $20 \times 20\,\text{cm}^2$, again at 95 cm from the target. The same field sizes were also simulated for the standard linac at 70 cm from the target. In both systems the field size was defined at the machine isocenter. The number of particle histories simulated in BEAM for the largest $20 \times 20\,\text{cm}^2$ field was 1.2 billion and other field sizes were scaled to yield a similar number of particles in the final phase space file. Dose distributions were then scored for these field sizes using an SSD of 110 cm, with the same dose scoring geometry, particle histories, and statistical uncertainty as above.

Additional BEAM simulations were run with the original flattening filter, the reshaped version, and without one using a $10 \times 10\,\text{cm}^2$ field size and a 110 cm SSD. To verify that reshaping of the flattening filters does not adversely affect the beam flatness, beam profiles were simulated at an SSD of 110 cm, a depth of 10 cm for 10x10 and $20 \times 20\,\text{cm}^2$ beams, for both 6 and 10 MV v2 systems. The flatness was calculated based on the AAPM TG-45 definition using the maximum and minimum dose in the central 80% of the profiles (Nath *et al* 1994):

$$\text{Flatness} = \frac{(D_{\max} - D_{\min})}{(D_{\max} + D_{\min})} \times 100\% \tag{1}$$

The beam symmetry will not be affected by reshaping the flattening filter because the Monte Carlo simulations assume the flattening filter is perfectly symmetric about the CAX.

For all simulations the global cut-off parameters of AP = PCUT = 0.01 MeV for photons and AE = ECUT = 0.521 MeV for electrons were used. In all BEAMnrc simulations, directional bremsstrahlung splitting was used with a splitting number of 1000. All the techniques used in these simulations were thoroughly benchmarked as discussed in Keyvanloo *et al* (2012).

3. Results and discussion

Pictures of the electron contamination paths tracked by the BEAMnrc simulations are generated by the EGS_Windows visualization package and displayed in figure 5. In figure 5(a) a

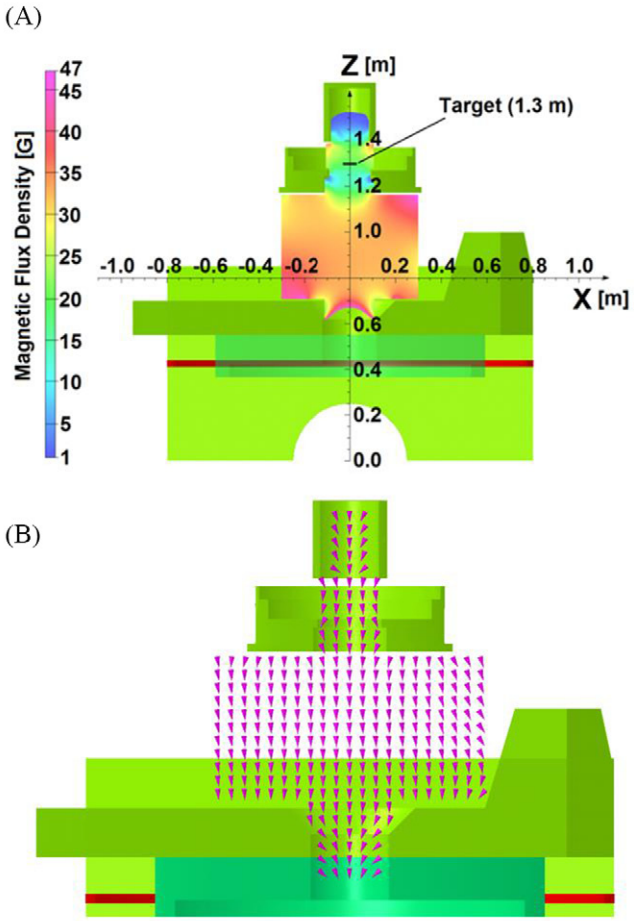

Figure 4. (A) Cross section of the magnet yoke with a superimposed magnetic field flux. This distribution (spanning between 1 and 47 G) covers the region along the photon beam between the linac and the surface of the yoke, as well as a widened region that covers the maximum extent of the MLC assembly. Axis labels are in units of meters. (B) Vector map showing the direction of the magnetic field vectors in the *X*-*Z* plane (similar field vectors in the *Y*-*Z* plane).

schematic of our v2 linac-MR geometry is displayed. Figures 5(b) and (c) show the electron paths in the absence ($B = 0$ T) and in the presence the MRI field, respectively. As is clear from these figures the confinement effect of the MRI fringe field of our v2 system on the contaminant electrons is very small. This is due to the very rapid decay of the fringe magnetic field outside the imaging volume dropping to approximately 0.0025 T at the location of the MLC. This is consistent with the observation that the increase in the skin dose for a phantom surface close to the bottom of the magnet pole (SSD = 100 cm, air gap = 5 cm) is very small (Keyvanloo *et al* 2012). As contaminant electrons enter the imaging volume of the linac-MR system they are already scattered and not significantly captured by the fringe field. At this point the main B-field (0.5 T) confines these electrons and direct them to the phantom surface leading to small increase in the surface dose. Any electron contamination generated in the

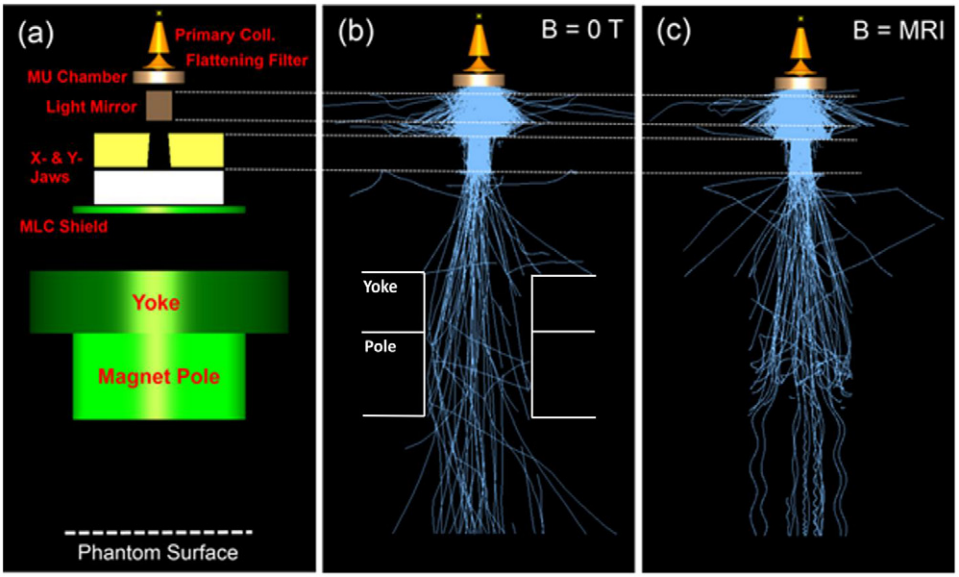

Figure 5. Visualization of the electron contamination paths for an SID of 120 cm and x-ray field size of 20 × 20 cm^2. To generate these, 10 000 initial particles were fired on the target from the phase space source. (a) The v2 Linac-MR geometry. (b) The electron paths in the absence of magnetic field ($B = 0$ T). (c) The electron paths in the presence of the 3D magnetic field of the v2 system. All electrons produced, including the ones at the base of the flattening filter, are tracked, however only electrons that travel past the flattening filter are shown.

air gap is captured and focused onto the CAX resulting to an increase in the skin dose with increased air gap.

Figure 6 shows the increase in skin dose with increasing air gap in both the 6 and 10 MV v2 models. The conventional 100 cm SSD models are not shown, because our previous work shows an insignificant increase in the surface dose with increasing air gap in the absence of a magnetic field (figure 8 in Keyvanloo *et al* (2012)). As the SSD is increased from 100 cm to 120 cm, the skin dose approximately doubles from 15.9% to 29.6% for the 6 MV and from 11.2% to 19.6% for the 10 MV. Thus, not only is the skin dose lower at all SSDs for the 10 MV, it also changes less rapidly with increasing SSD: this highlights a potential advantage of using 10 MV. Possible explanations for the reduced skin dose at 10 MV stem from the higher mean energy of the contaminant electrons which results in (1) a larger radius of curvature and consequently fewer electrons being confined and directed to the CAX and (2) these higher energy electrons traveling deeper and therefore contributing less dose to shallow depths.

A comparison of the dependence of the CAX skin dose on field size is made between 6 and 10 MV v2 linac-MR and conventional 6 and 10 MV linac models in figure 7. The increase in skin dose due to the magnetic field is 10.2% and 5.3% at 5 × 5 cm^2 for 6 and 10 MV, respectively. For larger field sizes the increases in skin dose due the magnetic field become smaller and for 10 MV at 20 × 20 cm^2 there is a reduction in the skin dose. We expect that this trend would continue for both 6 and 10 MV, with increasing reductions in skin dose in the presence of the magnetic field for larger field sizes. (For our v2 system the size of the hole in the yoke and pole plate limits the maximum field size to 20 × 20 cm^2, however). As explained in Keyvanloo *et al* (2012), with a small field size (collimation) there is a relatively large amount

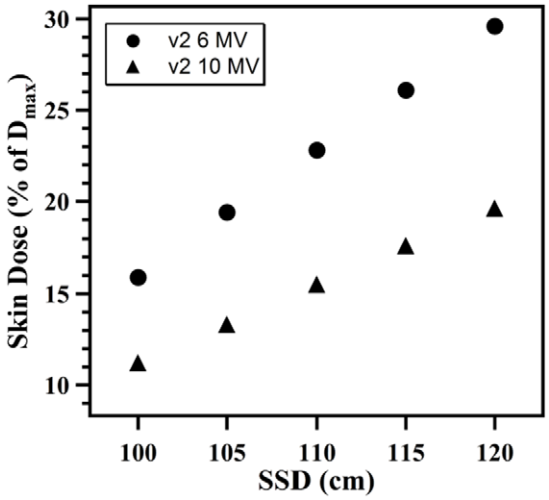

Figure 6. Comparison of the skin dose of the longitudinal v2 linac-MR system with the 0.5 T superconducting magnet for 6 and 10 MV linacs as a function of SSD. The SSDs of 100–120 cm correspond to the air gaps of 5–25 cm (field size of $10 \times 10\,cm^2$).

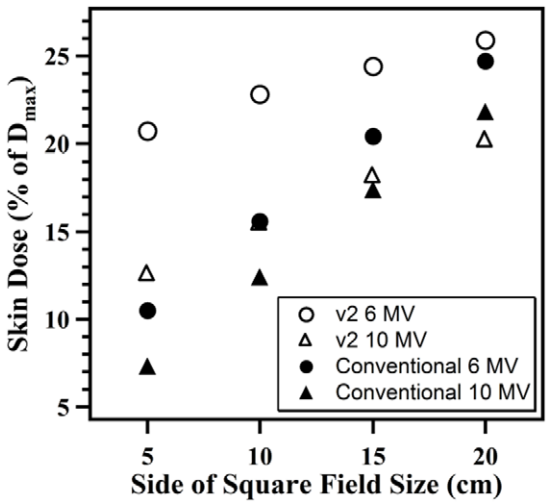

Figure 7. The skin dose of the longitudinal v2 linac-MR system with the 0.5 T superconducting magnet for 6 and 10 MV linacs as a function of the field size (air gap of 15 cm). Simulations of 6 MV and 10 MV beam models with conventional 100 cm SSD linac models are shown for comparison.

of contaminant electrons from the linac head that scatter off the jaws outside the field in the absence of the magnetic field, but in the presence of the longitudinal B-field these electrons are contained and contribute to the CAX skin dose. With a larger field size this increase is less pronounced, since relatively fewer of the magnetically contained contaminant electrons contribute to dose on the CAX. Beyond a certain field size, contaminant electrons scattered off the jaws that would reach the CAX with no B-field are now contained off the CAX and do not contribute to the CAX dose, thus reducing the CAX skin dose at larger field sizes.

Table 1. Dose rates and skin doses for conventional 600C and v2 linac-MR systems with the conventional 600C flattening filter and a new reshaped flattening filter (and SSD of 110 cm and $10 \times 10\,cm^2$ field size).

	Dose rate (MU min^{-1})	Skin dose (% of D_{max})
6 MV, 600C	600	15.6
6 MV, v2	355	22.8
6 MV, v2, reshaped flattening filter	529	25.4
10 MV, 600C	600	12.4
10 MV, v2	355	15.5
10 MV, v2, reshaped flattening filter	604	17.9

Table 2. Flatness of the beam profiles, at 10 cm depth, for 6 and 10 MV v2 linac-MR systems with the redesigned flattening filter.

	10×10 inline (%)	10×10 crossline (%)	20×20 inline (%)	20×20 crossline (%)
6 MV	2.1	2.2	1.9	2.0
10 MV	2.2	2.8	2.2	2.5

At the increased SAD (130 cm) of our v2 system a maximum dose rate of 355 MU min^{-1} can be achieved for a linac normally having a maximum output of 600 MU min^{-1} at 100 cm SAD. By removing the flattening filter, a maximum dose rate of 1090 MU min^{-1} could be achieved with our v2 linac-MR system. However, this removal comes at the cost of increased skin dose: for a $10 \times 10\,cm^2$ field at SSD = 110 cm the skin dose increases from ~22.8% with the standard flattening filter to ~35.7% with it removed. To mitigate the loss of dose rate while keeping the increase in the skin dose at minimum we redesigned the flattening filter as described in section 2.1. Results of this are summarized in table 1. For 6 MV there is a substantial increase in the DR, from 355 MU min^{-1} to 529 MU min^{-1}, and only an increase of 2.6% in the skin dose with the redesigned flattening filter with respect to the conventional flattening filter; this is small compared to the 12.9% increase when the flattening filter is removed. For 10 MV the trend is similar but the DR of the 600 MU min^{-1} is fully recovered with the redesigned flattening filter. In this case the increase in the skin dose is 2.4% with respect to the conventional flattening filter.

Beam flatness at 10 cm depth for both 6 and 10 MV v2 systems are summarized in table 2. Both inline (y-) and crossline (x-) profiles show that the beam is flat to within 3% over the central 80% of the profile, which is acceptable based on current QA recommendations (Klein *et al* 2009). This suggests that reshaping of the flattening filter maintains adequate beam flatness. It is important to note that these flattening filters were not optimized to the beam energy spectra as the purpose of this work was simply examining the changes to the skin dose.

4. Conclusions

The increase in the skin dose due to the longitudinal magnetic field of the v2 linac-MR systems depends on the SSD (air gap), the photon beam field size, and the beam energy. Our previous work showed that the surface dose for a conventional Varian 600C linac was 10–11% for various SSDs (figure 8 in Keyvanloo *et al* (2012)). For SSDs between 100 and 120 cm, increases in the skin dose range between ~6%–19% and ~1%–9% is seen for the 6 and 10 MV v2 systems, respectively. As the side of the square field is increased from 5 cm to 20 cm the

increase in the skin dose of the 6 MV v2 system varies from ~10.5% to ~1.5%; for the 10 MV v2 system the increase is ~6% for a $5 \times 5\,\mathrm{cm}^2$ field, while a decrease of ~1.5% is observed for a $20 \times 20\,\mathrm{cm}^2$ field. These results suggest that changes to the skin dose are not expected to be a limitation in the clinical use of the v2 systems. This also validates that the fringe field of the new magnet and yoke design does not produce clinically unacceptable skin dose. Further, the relatively lower skin dose increase seen at 10 MV offers a possible advantage in future designs of linac-MR prototypes.

An important result of this work is that the reduction in dose rate caused by the extended SSDs of these linac-MR systems can be overcome by reshaping the flattening filter while minimizing the increase in the skin dose. The proposed reshaped flattening filter increased the dose rate of the v2 systems from 355 MU min^{-1} with a conventional flattening filter, to 529 MU min^{-1} (6 MV) or 604 MU min^{-1} (10 MV). For both energies, the skin dose was increased by ~2.6% using this reshaped filter. Treatment times on the v2 linac-MR would then be comparable to current clinical linacs. Flattening filter redesign thus provides an effective method of recovering the dose rate lost due to the increased SAD of the v2 system while minimizing the increase in skin dose.

Acknowledgments

This research is partially supported by Alberta Innovations: Health Solutions, Alberta Cancer Foundation, and Western Economic Diversification (Canada).

References

Baillie D, St. Aubin J, Fallone B G and Steciw S 2015 FEM design and simulation of a short, 10 MV, S-band linac with Monte Carlo dose simulations *Med. Phys.* **40** 2044–53

Bielajew A F 1989 Electron transport in $\vec{E}$ and $\vec{B}$ field *Monte Carlo Transport of Electrons and Photons Below 50 MeV* ed T M Jenkins *et al* (New York: Plenum) pp 421–34

Bielajew A F 1993 The effect of strong longitudinal magnetic fields on dose deposition from electron and photon beams *Med. Phys.* **20** 1171–79

Brauer J R 2013 Appendix B: nonlinear B–H curves *Magnetic Actuators and Sensors* 2nd edn (Hoboken, NJ: Wiley)

Crijns S P M, Raaymakers B W and Lagendijk J J W 2012 Proof of concept of MRI-guided tracked radiation delivery: tracking 1D motion *Phys. Med. Biol.* **57** 7863–72

Fallone B G 2014 The rotating biplanar linac-magnetic resonance imaging system *Semin. Radiat. Oncol.* **24** 200–2

Fallone B G, Murray B, Rathee S, Stanescu T, Steciw S, Vidakovic S, Blosser E and Tymofichuk D 2009 First MR images obtained during mega-voltage photon irradiation from a prototype integrated linac-MR system *Med. Phys.* **36** 2084–8

Gloria N B S, Areiza M C L, Miranda I V J and Rebello J M A 2009 Development of a magnetic sensor for detection and sizing of internal pipeline corrosion defects *NDT E Int.* **42** 669–77

Heid O, Kleemann M and Heller J 2015 Integrated MRI-LINAC radiotherapy machine *Proc. Int Soc. Mag. Reson. Med.* **23** 3068

ICRP 1991 1990 Recommendations of the international commission on radiological protection. ICRP publication 60 *Ann. ICRP* **21** (1-3)

Kawrakow I and Rogers D W O 2003 The EGSnrc code system: Monte Carlo simulation of electron and photon transport *Report* No. PIRS-701 (Ottawa: National Research Council of Canada)

Keall P J, Barton M and Crozier S 2014 The Australian magnetic resonance imaging-linac program *Semin. Radiat. Oncol.* **24** 203–6

Kevyanloo A, Burke B, Warkentin B, Tadic T, Rathee S, Kirkby C, Santos D M and Fallone B G 2012 Skin dose in longitudinal and transverse linac-MRIs using Monte Carlo and realistic 3D MRI field models *Med. Phys.* **39** 6509–21

Kirkby C, Murray B, Rathee S and Fallone B G 2010 Lung dosimetry in a linac-MRI radiotherapy unit with a longitudinal magnetic field *Med. Phys.* **37** 4722–32

Kirkby C, Stanescu T, Rathee S, Carlone M, Murray B and Fallone B G 2008 Patient dosimetry for hybrid MRI-radiotherapy systems *Med. Phys.* **35** 1019–27

Klein E E *et al* 2009 Task group 142 report: quality assurance of medical accelerators *Med. Phys.* **36** 4197–212

Nath R, Biggs P J, Bova F J, Ling C C, Purdy J A, van de Geijn J and Weinhous M S 1994 AAPM code of practice for radiotherapy accelerators: report of AAPM radiation therapy task group no. 45 *Med. Phys.* **21** 1093–121

Oborn B M, Kolling S, Metcalfe P E, Crozier S, Litzenberg D W, Keall P J 2014 Electron contamination modeling and reduction in a 1 T open bore inline MRI-linac system *Med. Phys.* **41** 051708

Oborn B M, Metcalfe P E, Butson M J and Rosenfeld A B 2009 High resolution entry and exit Monte Carlo dose calculations from a linear accelerator 6 MV beam under the influence of transverse magnetic fields *Med. Phys.* **36** 3549–59

Oborn B M, Metcalfe P E, Butson M J and Rosenfeld A B 2010 Monte Carlo characterization of skin doses in 6 MV transverse field MRI-linac systems: effect of field size, surface orientation, magnetic field strength, and exit bolus *Med. Phys.* **37** 5208–16

Oborn B M, Metcalfe P E, Butson M J, Rosenfeld A B, Keall P J 2012 Electron contamination modeling and skin dose in 6 MV longitudinal field MRIgRT: impact of the MRI and MRI fringe field *Med. Phys.* **39** 874–90

Raaijmakers A J E, Raaymakers B W, van der Meer S and Lagendijk J J W 2007 Integrating a MRI scanner with a 6 MV radiotherapy accelerator: impact of the surface orientation on the entrance and exit dose due to the transverse magnetic fields *Phys. Med. Biol.* **52** 929–39

Raaijmakers A J, Raaymakers B W and Lagendijk J J 2005 Integrating a MRI scanner with a 6 MV radiotherapy accelerator: dose increase at tissue-air interfaces in a lateral magnetic field due to returning electrons *Phys. Med. Biol.* **50** 1363–76

Raaijmakers A J, Raaymakers B W and Lagendijk J J 2008 Magnetic-field-induced dose effects in MR-guided radiotherapy systems: dependence on the magnetic field strength *Phys. Med. Biol.* **53** 909–23

Raaymakers B W *et al* 2009 Integrating a 1.5 T MRI scanner with a 6 MV accelerator: proof of concept *Phys. Med. Biol.* **54** N229–37

Raaymakers B W, Raaijmakers A J, Kotte A N, Jette D and Lagendijk J J 2004 Integrating a MRI scanner with a 6 MV radiotherapy accelerator: dose deposition in a transverse magnetic field *Phys. Med. Biol.* **49** 4109–18

Rogers D W O, Walters B and Kawrakow I 2005 *Report* No. PIRS-0509(A)rev I (Ottawa: National Research Council of Canada)

Santos D M, St. Aubin J, Fallone B G and Steciw S 2012 Magnetic shielding investigation for a 6 MV in-line linac within the parallel configuration of a linac-MR system *Med. Phys.* **39** 788–9

St. Aubin J, Steciw S, Kirkby C and Fallone B G 2010b An integrated 6 MV linear accelerator model from electron gun to dose in a water tank *Med. Phys.* **37** 2279–88

St. Aubin J, Santos D M, Steciw S and Fallone B G 2010a Effect of longitudinal magnetic fields on a simulated in-line 6 MV linac *Med. Phys.* **37** 4916–23

Treurniet J A and Rogers D W O 1999 EGS Windows 4.0 User's Manual *Report* PIRS-0669 (Ottawa: National Research Council of Canada)

Van Heijst T C F, den Hartogh M D, Lagendijk J J W, van den Bongard H J G D and van Asselen B 2013 MR-guided breast radiotherapy: feasibility and magnetic field impact on skin dose *Phys. Med. Biol.* **58** 5917–30

Walters B, Kawrakow I and Rogers D W O 2005 *Report* No.PIRS-794rev B (Ottawa: National Research Council of Canada)